

Density Functional Theory Study of Th-doped LiCAF and LiSAF for Nuclear Clock Applications

Martin Pimon,¹ Tobias Kirschbaum,² Thorsten Schumm,³ Adriana Pálffy,² and Andreas Grüneis¹

¹*Institute for Theoretical Physics, TU Wien, Wiedner Hauptstrasse 8-10/E136, 1040 Vienna, Austria*

²*University of Würzburg, Institute of Theoretical Physics and Astrophysics, Am Hubland, 97074 Würzburg, Germany*

³*Institute for Atomic and Subatomic Physics, TU Wien, Stadionallee 2, 1020 Vienna, Austria*

(Dated: July 15, 2025)

Thorium-doped LiCaAlF₆ and LiSrAlF₆ (Th:LiCAF and Th:LiSAF) are promising crystals for a solid-state nuclear clock based on the 8 eV transition in ²²⁹Th; however, their complex crystal structures complicate understanding the atomic arrangement of the thorium defects. In this work, density functional theory simulations are employed to systematically investigate these systems, including temperature-dependent effects and environmental conditions of fluorine saturation and deficiency. We investigated 20 distinct charge compensation schemes for each material, revealing lower defect formation energies in Th:LiSAF than in Th:LiCAF. This suggests that the former may attain a higher concentration of thorium nuclei. Furthermore, we calculated the electric field gradient for the lowest energy structure per compensation pathway. Our investigation shows that results previously reported in the literature apply only to a subset of experimental conditions.

I. INTRODUCTION

The thorium-229 isotope has an exceptionally low-energy first nuclear excited state [1]. Recently, Zhang et al. [2] performed high-precision laser spectroscopy of ²²⁹Th nuclei doped in CaF₂ and reported a transition energy of 8.355 732 812 685(8) eV above the ground state. Due to its narrow line width, this transition is a candidate for a new frequency reference standard [3–5] and its practical implementation is commonly referred to as *nuclear clock* [6–8]. Its unprecedented sensitivity to temporal variations of fundamental constants and dark matter candidates is predicted to enable exploration of physics beyond the Standard Model [9–13].

Attempts to directly excite the nucleus in neutral atoms by laser irradiation would inadvertently lead to ionization since the first ionization potential of Th is 6.3 eV and thus lower than the transition to the nuclear isomer [14]. One way to remove outer shell electrons and simultaneously increase the number of Th nuclei in the target is to form an ionic solid with thorium and other elements. Because the scarcity of the isotope makes single-crystal growth impractical [8], doping it into bulk insulators that are transparent to the isomeric transition wavelength is a more viable solution [15]. For this purpose, several large-band gap host crystals have been proposed [16], and a few have been successfully grown and tested experimentally: Th:CaF₂, Th:MgF₂, and Th:LiSrAlF₆ (Th:LiSAF) [2, 17–19].

Numerical simulations are essential for gaining insights into the microscopic structure of defects in such crystals, enabling calculation of nuclear sub-level splitting caused by an interaction with the Electric Field Gradient (EFG) at the thorium position and the nuclear quadrupole moment. Additionally, calculating the defect formation energy for various structures provides the thermodynamic probability of these structures occurring during crystal growth.

For various defect configurations of Th:CaF₂ and Th:MgF₂, EFG values and defect formation energies were calculated using Density Functional Theory (DFT) [20–22]. The number of viable defect configurations in these binary hosts is limited compared to the quaternary hosts LiSAF and LiCAF, making their defect structures more difficult to predict. Jackson *et al.* [23] performed the initial investigation into these systems using a classical potential. Pimon *et al.* [24] simulated Th:LiCAF using DFT, providing defect formation energies, evaluated using a canonical ensemble. Another DFT study of Th:LiSAF based on the data generated in Ref. [24] reported the lowest energy structure, but did not publish its defect formation energy [18].

With the present study, we aim to improve previous research on Th:LiSAF and Th:LiCAF in three key ways: Firstly, we aim at an unbiased approach by generating a large set of structural configurations for the Th:LiSAF system. Secondly, we report defect formation energies of the various charge compensation schemes in Th:LiSAF and go beyond those reported for Th:LiCAF [24] by considering tunable chemical potentials in the grand canonical ensemble and including temperature dependence. Thirdly, we present the electric field gradients for the lowest energy structures per charge compensation scheme for both materials.

II. METHODS

We follow the approach outlined in Freysoldt et al. [25] to calculate defect formation energies. A breakdown of the complete workflow in this study is as follows: A. We compile a list of compounds in the Li-Ca(Sr)-Al-F-Th system. B. We calculate the chemical potentials of these elements. C. We generate a list of potential charge compensation schemes in Th:LiSAF, generate defect structures for each compensation scheme, and calculate their

electronic internal energies. Together with the dataset from Ref. [24], we only select the defect structures with the lowest energy per compensation scheme and calculate the vibrational contribution to their free energy. D. We simulate a lower doping concentration for each structure to obtain a correction in the dilute doping limit and to calculate the electric field gradient on thorium. E. We determine the defect formation energy for each structure under different experimental conditions.

A. Compound Selection

We select compounds comprising combinations of cations Li, Ca, Sr, Al, and Th with anions F that have been experimentally observed and characterized. We gather structural data for the solid phases by querying the Materials Project database [26–28] and cross-validate the results with the Inorganic Crystal Structure Database [29]. Due to the impracticality of an exhaustive analysis encompassing all possible combinations, we restrict our search to fluorides because of their similarity to thorium-doped LiCAF and LiSAF. In cases of phase transitions, we utilize the stable phase determined by DFT simulations at 0 K. We further include metastable compounds slightly above the convex hull [30] to restrict the chemical potential domain, and we also include metallic elementary phases to define the upper bound of their element’s chemical potential (see Sec. IIB).

We now list all compounds considered in this study. The single-component metals Li, Ca, Sr, Al, and Th; the compounds LiF, CaF₂ (SrF₂), and AlF₃ are the constituents of the host crystal LiCAF (LiSAF), along with ThF₄ to create the defect. Li₃AlF₆, LiThF₅, and Li₃ThF₇ contain neither Ca nor Sr. CaAlF₅, and Ca₂AlF₇ contain Ca but not Sr, whereas SrAlF₅ and Sr₅Al₂F₁₆ contain Sr but not Ca. Finally, F₂ is the only gaseous phase we include.

B. Calculation of Chemical Potentials

The crystals are typically grown at ambient pressure and melting temperature of the host materials (1082 K for LiCAF and 1038 K for LiSAF) and cooled slowly [31, 32]. Thus, the appropriate thermodynamic potential to describe the process is the Gibbs free energy $G(T) = \mu(T)N = F(T) + pV(T)$, where T represents absolute temperature, μ is the chemical potential, N is the number of formula units per unit cell, F is the Helmholtz free energy, $p = 1$ atm is pressure, and V is the unit cell volume.

When simulating solid phases, we calculate the Helmholtz free energy $F(T) = U_{\text{el}} + U_{\text{vib}} - TS_{\text{vib}}(T)$, where we obtain the electronic internal energy U_{el} from DFT calculations, and the vibrational zero point energy U_{vib} , together with the vibrational entropy S_{vib} from a frozen phonon simulation [33, 34]. We neglect the elec-

tronic contribution to the entropy, which is only relevant for metallic phases in the temperature range of this study. Also note that the impact of thermal volume expansion work on the total energy is negligible, and we disregard it by fixing the cell volumes to the DFT equilibrium values $pV(T) = pV_{\text{DFT}}$.

For the gaseous F₂ phase, we calculate the entropy as $S = S_{\text{trans}} + S_{\text{vib}} + S_{\text{rot}}$. We use the Sackur-Tetrode equation for the translational part S_{trans} , the entropy of the quantum harmonic oscillator for the vibrational part S_{vib} , and the entropy of the quantum rigid rotor for the rotational part S_{rot} (see also Appendix B). To this end, we calculate the fundamental vibrational frequency and the equilibrium bond length with DFT, and use $m_{\text{F}} = 18.998$ Da [35]. In addition, we include volume expansion work by applying the ideal gas law $pV(T) = Nk_{\text{B}}T$.

We calculate the chemical potentials of the elements Li, Sr, Ca, Al, F, and Th by solving a system of inequalities

$$\begin{aligned} \mu_{\text{Li}} + \mu_{\text{Ca}} + \mu_{\text{Al}} + 6\mu_{\text{F}} &= \mu_{\text{LiCAF}}, \\ \mu_{\text{Th}} + 4\mu_{\text{F}} &= \mu_{\text{ThF}_4}, \\ \mu_{\text{Li}} &\leq \mu_{\text{Li}}[\text{metal}], \\ &\vdots \\ \mu_{\text{F}} &\leq \mu_{\text{F}_2}[\text{gas}]/2, \\ \mu_{\text{Li}} + \mu_{\text{F}} &\leq \mu_{\text{LiF}}, \\ &\vdots \end{aligned} \tag{1}$$

The chemical potential of a compound cannot exceed that of its allotrope; the first equality relation thus confines the chemical environment to that of the host crystal. The second equality fixes the chemical potential of thorium. For the same reason, the chemical potential of each species cannot be larger than its elementary allotrope’s, but it can always be smaller. The remaining inequalities provide information about the chemical potential of each species within various compounds. Consequently, these relations may restrict the codomain for the chemical potential of a species. We then employ a numerical routine that finds the solution for all μ_i under two conditions: maximizing and minimizing μ_{F} , corresponding to fluoride saturation and deficiency. We chose these conditions because crystal growth was performed in a fluorinated atmosphere in thorium-doped calcium fluoride to enhance transmission properties [36].

C. Charge Compensation Schemes

In examining potential charge compensation mechanisms and initial defect geometries, we adopt an approach analogous to that outlined in Ref. [24]. In essence, our strategy involves imposing a constraint on the number of atoms of a particular species n_i , with $i \in \{\text{Li, Ca, Sr, Al, F, Th}\}$, that are introduced ($n_i > 0$) and removed ($n_i < 0$) from the crystal lattice to form the defect, with a limit of five such atoms ($\sum_i |n_i| = 5$).

Intending to generate supercells with lattice vectors of comparable magnitude, we use $2 \times 2 \times 1$ primitive unit cells of the host crystals, resulting in 80 host atoms. When thorium substitutes an atom in the cell, it results in an imbalance between its number of valence electrons ($= 4$) and that of the substituted atom. We assume the defect is closed-shell and fully compensated by vacancies or interstitials, constrained to be near the thorium defect. We initially place interstitial atoms on high-symmetry Wyckoff positions. The maximal distance parameter controls the number of atomic arrangements. We aim to generate at least 20 symmetrically unique structures for each of the 20 assessed charge compensation mechanisms. In total, we generate 1812 structures for Th:LiSAF and use 1567 structures for Th:LiCAF [24].

We then perform relaxations on these supercells. When interatomic forces are smaller than $10 \text{ meV } \text{\AA}^{-1}$, we compare the internal energies associated with each charge compensation scheme and select the structure corresponding to the lowest energy state. Subsequently, we calculate the vibrational Helmholtz free energy for the selected structures, incorporating a non-analytical term correction for insulators derived from the Born effective charges and the static dielectric tensor [37–39].

D. Dilute Doping Limit

In practice, the defect concentration is low enough to simplify the system to the dilute doping limit. To address this, we correct the electronic internal energy of the $2 \times 2 \times 1$ supercells by simulating a larger supercell with $4 \times 4 \times 2$ repetitions of the primitive unit cell (640 host atoms). After inserting the smaller (doped, relaxed) structure into the larger (pristine) supercell, we perform another relaxation of the system. Then, we apply a correction to the electronic internal energy $E_{\text{corr}} = U_{\text{el}}[X_{4 \times 4 \times 2}] - U_{\text{el}}[X_{2 \times 2 \times 1}] - 7U_{\text{el}}[\text{bulk}_{2 \times 2 \times 1}]$, where X denotes the supercell containing the thorium defect and “bulk” the pristine host crystal. In the larger supercell, we also compute the electric field gradient $V_{ij} = \frac{\partial^2 V}{\partial x_i \partial x_j}$ at the site occupied by thorium.

E. Defect Formation Energies

Under the conditions and approximations described above, the defect formation energy is [25]

$$G^f[X](T) = F[X](T) - F[\text{bulk}](T) - \sum_i n_i \mu_i(T) + E_{\text{corr}}, \quad (2)$$

where G^f is the Gibbs free energy of formation, F is the Helmholtz free energy including the electronic internal energy and vibrational contributions, n_i is the number of atoms removed or added to the supercell X to form the defect, μ_i is the chemical potential for the respective

element i , and E_{corr} is the correction term to account for the dilute doping limit.

F. Computational Details

We employ the Vienna Ab-initio Simulation Package (VASP) [40–44] version 6.4.3 to compute internal electronic energies and interatomic forces using the approximation to the exchange-correlation potential by Perdew *et al.* [45] (PBE). We utilize the pseudopotentials `Li_sv_GW`, `Ca_sv_GW`, `Sr_sv_GW`, `Al_GW`, `Th`, and `F_h_GW`.

For pristine crystals, we implement a convergence study by adjusting both the k -mesh, energy cutoff, and cell volume until they reach a convergence threshold of $\Delta U_{\text{el}} \leq 1 \text{ meV/atom}$ compared to the most accurate calculation. We evaluate doped supercells only at the Γ -point in k -space. When calculating Born effective charges and the static dielectric tensor for doped and pristine crystals, we increase the k -space sampling by doubling the number of points in each direction. We conducted the calculations of Th:LiCAF and Th:LiSAF with the plane wave basis set having a cutoff of 950 eV.

We calculated vibrational properties using phonopy [33, 34] version 2.21.2 in the frozen phonon approach in the harmonic approximation, targeting supercells with lattice vectors of approximately equal length and containing at least around 100 atoms.

We implemented many parts of the workflow using AiIDA [46–48] (aiida-core version 2.5.1 with the plugins aiida-vasp [49] (version 3.1.0) and aiida-phonopy [50, 51] (version 1.1.4)).

III. RESULTS

To briefly describe the stoichiometry for each compensation scheme, we use a notation for the numbers n_i : The order of the elements i is Li, Ca (Sr), Al, F, and Th; a bar indicates a negative sign. To give an example, 02001 corresponds to the removal of two Ca (Sr) atoms, and the addition of one Th atom ($\text{Th}_{\text{Ca}}^{\bullet\bullet} + \text{v}_{\text{Ca}}''$ in Kröger-Vink notation [52]). We use the shorthand notation when a concise representation is advantageous, and Kröger-Vink notation when conveying more detailed information about the defect structure.

Fig. 1 shows the temperature-dependent defect formation energies for the lowest energy structure per charge compensation scheme for Th:LiCAF and Th:LiSAF. See also the Appendix for a breakdown of different energy contributions. Table I presents the calculated and diagonalized EFG values, following the standard convention: $|V_{zz}| \geq |V_{yy}| \geq |V_{xx}|$ and $\eta = \frac{V_{xx} - V_{yy}}{V_{zz}}$.

For the Th:LiCAF system, we identify one dominant charge compensation pathway $\text{Th}_{\text{Ca}}^{\bullet\bullet} + 2\text{v}_{\text{Li}}'$ in fluoride saturated environments, and two alternative schemes $\text{Th}_{\text{Ca}}^{\bullet\bullet} + \text{Li}_{\text{Al}}''$, and $\text{Th}_{\text{Al}}^{\bullet} + \text{v}_{\text{Li}}'$ that emerge in a fluoride-deficient environment. In Th:LiSAF, the dominant

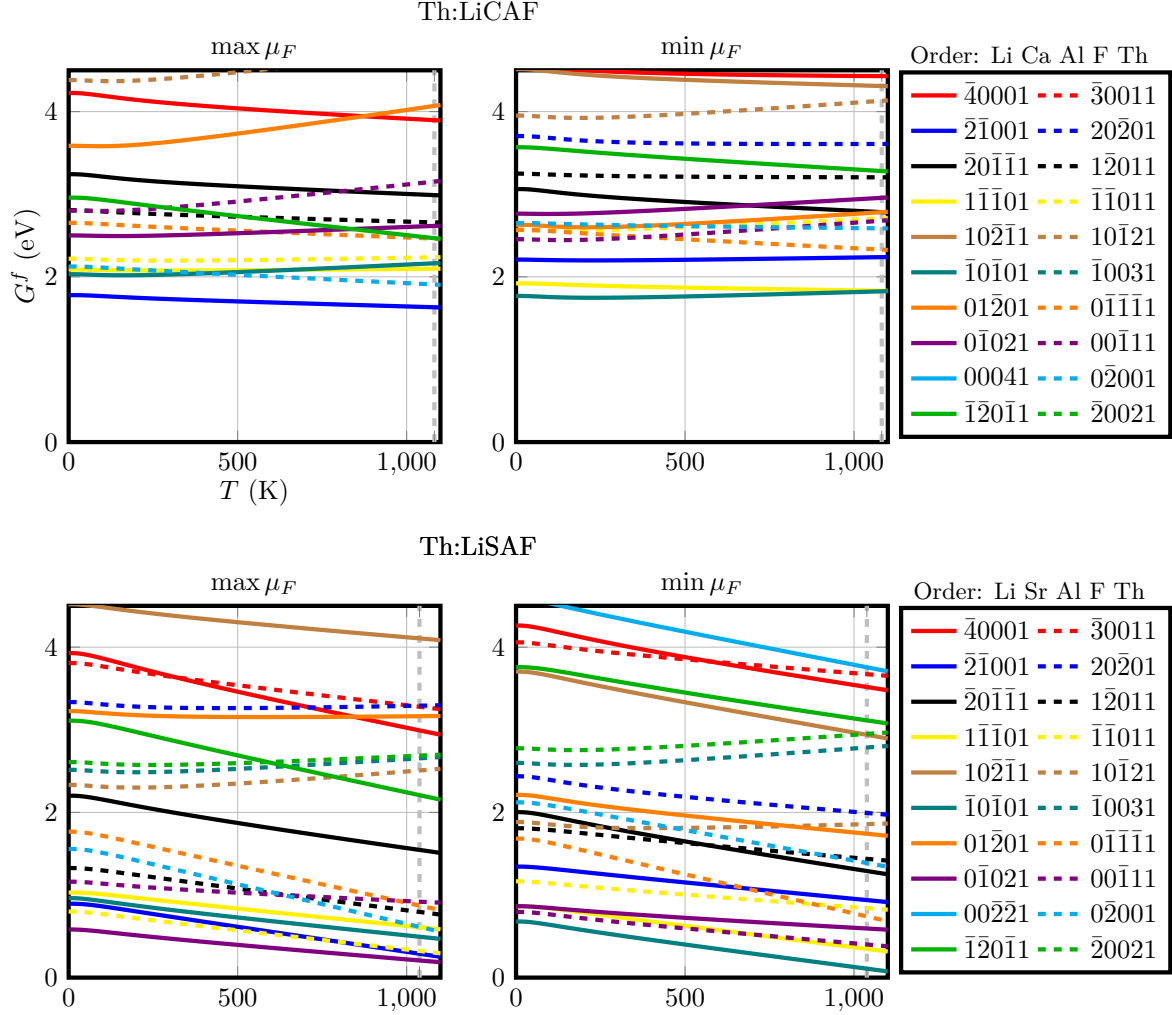


FIG. 1. Defect formation energy of the lowest energy structure per compensation scheme in Th:LiCAF (top row) and Th:LiSAF (bottom row). A maximum threshold of 4.5 eV is imposed for improved visibility of the more relevant compensation schemes. Dashed vertical lines indicate the host crystal's melting point. Left: μ_F maximized. Right: μ_F minimized.

scheme is $\text{Th}_{\text{Sr}}^{\bullet\bullet} + 2\text{F}_i''$ in fluoride saturated environments with other schemes, such as $\text{Th}_{\text{Sr}}^{\bullet\bullet} + \text{v}_{\text{Li}}' + \text{F}_i'$ and $\text{Th}_{\text{Sr}}^{\bullet\bullet} + 2\text{v}_{\text{Li}}'$ also appearing at lower energies, with a larger temperature dependence. In fluoride deficiency, the $\text{Th}_{\text{Al}}^{\bullet} + \text{v}_{\text{Li}}'$ scheme seems to emerge with $\text{Th}_{\text{Sr}}^{\bullet\bullet} + \text{Li}_{\text{Al}}''$, $\text{Th}_{\text{Al}}^{\bullet} + \text{F}_i'$, and $\text{Th}_{\text{Sr}}^{\bullet\bullet} + 2\text{F}_i'$ having a similar formation energy at lower temperatures.

IV. DISCUSSION

Contrary to previous findings in the canonical ensemble [18, 24], our investigation reveals that $\text{Th}_{\text{Ca}}^{\bullet\bullet} + \text{v}_{\text{Li}}'$ and $\text{Th}_{\text{Sr}}^{\bullet\bullet} + 2\text{F}_i'$ are not universally lowest-energy compensation schemes, but rather in specific conditions — fluoride-deficient environments for Th:LiCAF and fluoride-saturated environments for Th:LiSAF. We further find that thorium substitution of Ca or Sr appears to be energetically favored in fluoride-saturated conditions.

The low defect formation energy of Th:LiSAF indicates that this material can accommodate a higher concentration of thorium defects compared to Th:LiCAF. The equilibrium defect concentration at a given temperature in the dilute doping limit is $c(T) = ge^{-G^f/k_B T}$, where g is a configurational degeneracy factor [25]. g depends on the defect symmetry and is generally distinct for each structure. For example, the lowest energy structures of Th:LiCAF and Th:LiSAF in fluoride-deficient environments, $\text{Th}_{\text{Al}}^{\bullet} + \text{v}_{\text{Li}}'$, show $g = 3$.

Taking the ratio of defect concentrations for these favored compensation schemes at the melting temperatures of LiCAF and LiSAF we find $c_{\text{LiCAF}}^{\text{Th:LiCAF}}(1082\text{ K})/c_{\text{LiSAF}}^{\text{Th:LiSAF}}(1032\text{ K}) \approx 10^{-8}$, suggesting a remarkably larger maximal thorium concentration in Th:LiSAF. However, it is essential to note that these values are subject to limitations, including kinetic barriers and systematic errors in DFT calculations. As our approach neglects the impact of ionic mobility, the defect

TABLE I. V_{zz} and η components of the electric field gradient at the thorium site of the lowest energy structure per charge compensation scheme.

Comp.	Th:LiCAF		Th:LiSAF	
	V_{zz} ($\text{V}/\text{\AA}^2$)	η	V_{zz} ($\text{V}/\text{\AA}^2$)	η
11011	382.90	0.72	373.70	0.82
10211	121.68	0.74	-184.60	0.90
21001	-133.43	0.69	-158.29	0.51
02001	113.99	0.21	-190.00	0.58
12011	-136.45	0.57	159.39	0.46
20111	-369.14	0.72	-466.98	0.83
01111	-141.54	0.30	-113.55	0.78
10121	318.92	0.54	-169.54	0.55
10031	210.81	0.06	-306.92	0.65
11101	-114.08	0.75	-85.91	0.63
10101	-386.16	0.06	-522.28	0.26
01201	-109.50	0.58	-219.96	0.66
00111	183.30	0.96	259.76	0.12
20021	-468.91	0.62	-475.21	0.72
30011	-254.55	0.40	-212.07	0.51
12011	-368.93	0.52	412.18	0.62
40001	433.00	0.92	118.52	0.71
20201	125.60	0.89	159.22	0.72
01021	-126.82	0.68	-102.41	0.81
00221	—	—	255.19	0.92
00041	-321.19	0.31	—	—

concentration of compensation schemes relying on small-ion diffusion could be underestimated when considering the defect formation energy alone. In addition, as shown in Appendix C, DFT is prone to inaccuracies exacerbated by the exponential term in $c(T)$. Also note that the dilute doping approximation is invalid for our results of the Th:LiSAF system at elevated temperatures due to the low defect formation energy of the favored scheme. While these limitations suggest that the calculated figure might not be exact, the relative advantage of Th:LiSAF in accommodating thorium atoms remains a valid conclusion of our results.

An open question remains regarding the adequacy of the compound selection in accurately restricting the chemical potentials. It is likely that other compounds not yet included in the database, or structures that have not been experimentally characterized, will impose further bounds on the chemical potentials. However, we wish to highlight the energy differences involved. Given the relatively small energy difference between the same compensation scheme in the two experimental conditions (≈ 0.3 eV) and the range of calculated defect formation energies (exceeding 1 eV), our analysis provides insights for understanding the potential charge compensation schemes for low-energy defects in Th:LiSAF, despite the limitation of an insufficiently explored phase space.

The EFG values presented in Table I enable distinguishing between potential defect structures based on excitation wavelength when using narrow-band laser sources. However, it is worth noting that our analysis focuses solely on the lowest energy structure per compen-

sation scheme and omits configurations with comparable low energies.

An apparent difference from EFG values on thorium reported for Th:CaF₂ [20] is the observed greater asymmetry values in Th:LiCAF and Th:LiSAF, which can be attributed to the lower symmetry characteristic of these trigonal materials compared to cubic CaF₂.

In conclusion, our DFT calculations reveal that Th:LiSAF exhibits lower defect formation energies than Th:LiCAF in the grand canonical ensemble, enabling higher doping concentrations. Notably, charge compensation schemes depend on fluorine saturation or deficiency. Our findings align with previous studies for specific conditions: fluorine saturation in Th:LiSAF and fluorine deficiency in Th:LiCAF [18, 24]. We also report EFG values for the lowest energy structure of each charge compensation mechanism.

Our simulations show that due to the numerous possibilities of charge compensation in thorium-doped LiCAF and LiSAF, growing a specific defect structure with desired properties preferentially may be possible by tuning experimental conditions. The selective promotion of defect structures that enhance the electronic bridge effect, where an electron couples to the nucleus, increasing its (de-)excitation rate, is particularly intriguing, as it could lead to significant improvements in the performance of solid-state nuclear clocks [53, 54]. In a companion publication [55], we investigate this concept by comparing electronic bridge transition rates for distinct low-energy charge compensation schemes.

ACKNOWLEDGMENTS

This research was supported by the Austrian Science Fund (FWF) [grant DOI:10.55776/F1004] (COMB.AT) together with the Deutsche Forschungsgemeinschaft (DFG, German Science Foundation) (PA 2508/5-1). A.P. gratefully acknowledges support from the DFG in the framework of the Heisenberg Program (PA 2508/3-1). This work has been funded by the European Research Council (ERC) under the European Union's Horizon 2020 and Horizon Europe research and innovation programme (Grant Agreement No. 856415 and No. 101087184). The computational results have been achieved using the Austrian Scientific Computing (ASC) infrastructure.

Appendix A: Defect Formation Energy

This section provides an overview of our approach to calculating defect formation energies. Table II presents a summary of calculated electronic energies U_{el} and the correction terms E_{corr} for the lowest energy structural configuration per compensation scheme. Fig. 2 displays the corresponding vibrational Helmholtz free energies

TABLE II. Electronic energies $U_{\text{el}}[X_{2 \times 2 \times 1}]$ and size correction terms E_{corr} for the lowest energy structure of each compensation scheme.

comp.	LiCAF		LiSAF	
	U_{el} (eV)	E_{corr} (eV)	U_{el} (eV)	E_{corr} (eV)
bulk	-460.485		-456.785	
$\bar{1}\bar{1}011$	-459.589	-0.078	-456.970	-0.790
$10\bar{2}\bar{1}1$	-456.965	1.426	-453.636	1.141
$\bar{2}\bar{1}001$	-448.428	-0.094	-445.220	-0.862
$0\bar{2}001$	-448.908	0.204	-445.949	-0.452
$\bar{1}\bar{2}0\bar{1}1$	-436.573	0.261	-433.494	0.219
$\bar{2}0\bar{1}\bar{1}1$	-446.401	0.124	-443.032	-0.477
$0\bar{1}\bar{1}\bar{1}1$	-447.398	0.051	-443.895	-1.012
$10\bar{1}21$	-479.700	-0.218	-477.348	-0.863
$\bar{1}0031$	-477.997	-0.482	-476.618	-1.686
$1\bar{1}\bar{1}01$	-459.479	-0.012	-456.497	-0.730
$\bar{1}0\bar{1}01$	-458.770	-0.283	-455.327	-0.999
$01\bar{2}01$	-467.960	-0.363	-463.505	-0.898
$00\bar{1}11$	-469.659	-0.224	-466.842	-0.860
$\bar{2}0021$	-467.096	0.513	-465.935	-0.705
$\bar{3}0011$	-456.596	0.312	-453.996	0.204
$\bar{1}\bar{2}011$	-459.457	-0.150	-457.663	-0.540
$\bar{4}0001$	-445.328	-0.231	-441.296	-0.782
$20\bar{2}01$	-468.098	0.234	-465.151	-0.169
$0\bar{1}021$	-470.684	-0.284	-468.584	-0.965
00041	-488.677	0.135	—	—
$00\bar{2}\bar{2}1$	—	—	-442.137	2.006

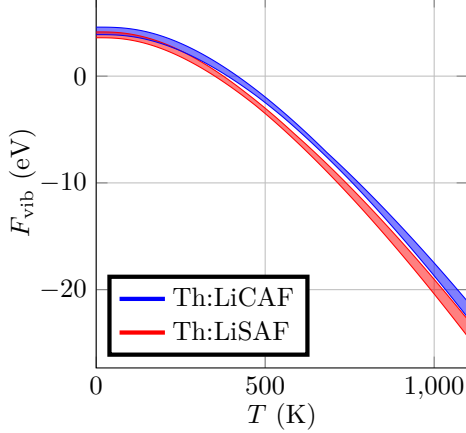


FIG. 2. Ranges of vibrational Helmholtz free energies for the lowest energy structures of each charge compensation scheme.

F_{vib} , which exhibit comparable values across the entire temperature range for all structural configurations. Fig. 3 depicts the chemical potentials under the two tuning scenarios. μ_{F} attains its highest possible value when maximized. In contrast, its minimization leads to μ_{Al} reaching its maximum value, accompanied by large values for the μ_i of the other cations.

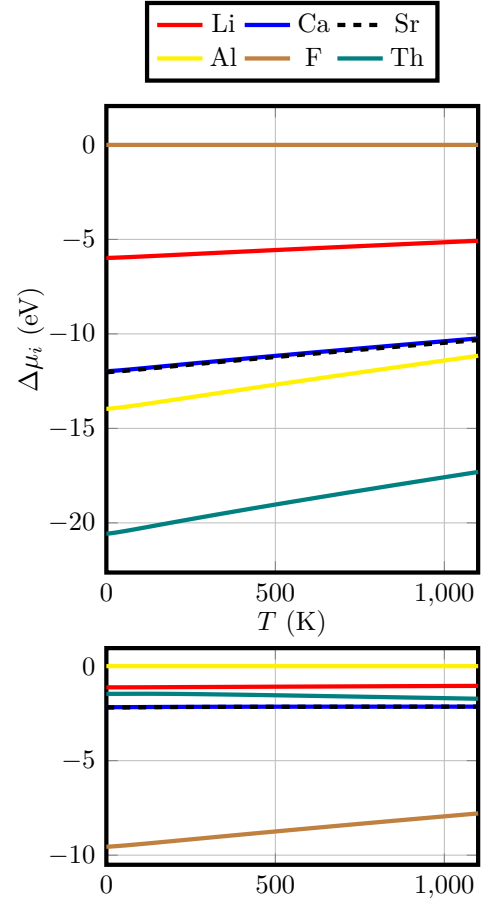


FIG. 3. Tuned chemical potentials, free from the pseudopotential reference $\Delta\mu_i = \mu_i - \mu_i[\text{bulk}]$. Top: μ_{F} maximized. Bottom: μ_{F} minimized.

Appendix B: Chemical Potentials

This section provides additional information on the tuning procedure for the chemical potentials. Table III lists the equilibrium lattice parameters of the standard conventional unit cell for all considered compounds. The table also includes the electronic energy U_{el} and the pressure-volume term.

We utilize the phonopy code for solids to determine the vibrational contributions to the Gibbs free energy (see Fig. 4) and employ standard thermodynamic expressions for the gaseous F_2 phase to calculate the corresponding Gibbs free energy, where the total entropy is a sum of the three components $S = S_{\text{trans}} + S_{\text{rot}} + S_{\text{vib}}$. We derive the translational contribution using the Sackur-Tetrode equation $S_{\text{trans}} = k_B \left(\frac{5}{2} + \ln \frac{k_B T}{p V_Q} \right)$, and the quantum volume $V_Q = \left(\frac{2\pi\hbar^2}{2m_F k_B T} \right)^{\frac{3}{2}}$. The rotational term is the solution to the quantum rigid rotor $S_{\text{rot}} = k_B \log \frac{2B_0}{k_B T}$, where $B_0 = \frac{\hbar^2}{m_F r_{\text{F}_2}^2}$, and r_{F_2} is the equilibrium bond length of the F_2 molecule. For the vibrational part,

TABLE III. Optimized lattice parameters, energy per formula unit U_{el} and pressure-volume term for the selected compounds.

Formula	Lattice	a (Å)	b (Å)	c (Å)	β	U_{el} (eV)	pV (meV)
Li	cubic	3.43				-3.69	0.01
Ca	cubic	5.52				-6.85	0.03
Sr	cubic	6.03				-6.36	0.03
Al	cubic	4.04				-3.75	0.01
F ₂	gas					-3.71	$k_B T$
Th	cubic	5.05				-7.44	0.02
LiF	cubic	4.08				-11.43	0.01
CaF ₂	cubic	5.50				-22.32	0.03
SrF ₂	cubic	5.86				-21.84	0.03
AlF ₃	rhombohedral	5.11			57.91	-23.42	0.03
ThF ₄	monoclinic	13.16	11.10	8.60	126.31	-35.49	0.05
LiCaAlF ₆	hexagonal	5.08		9.75		-57.56	0.07
LiSrAlF ₆	hexagonal	5.17		10.37		-57.10	0.08
Li ₃ AlF ₆	monoclinic	14.46	8.53	10.05	94.11	-58.11	0.07
LiThF ₅	tetragonal	15.24		6.71		-46.98	0.06
Li ₃ ThF ₇	tetragonal	6.95		12.26		-67.56	0.09
CaAlF ₅	monoclinic	8.82	6.41	7.44	115.03	-45.86	0.06
Ca ₂ AlF ₇	orthorhombic	7.04	7.72	9.60		-68.14	0.08
SrAlF ₅	tetragonal	20.20		14.54		-45.43	0.06
Sr ₅ Al ₂ F ₁₆	orthorhombic	7.59	12.61	14.30		-156.38	0.43

we use the solution of the quantum harmonic oscillator $S_{vib} = k_B \log \left(1 - e^{-\frac{\hbar\omega}{k_B T}} \right)$.

The fluorine atom mass is our only experimentally determined quantity, which we take as 18.998 Da [35]. We compute the vibrational frequency and molecular bond length to be $\nu = 29.882$ THz and $r_{F_2} = 1.413$ Å, respectively. In Fig. 5 we compare the three contributions to the Helmholtz free energy. Completing our calculation, we add the electronic internal energy U_{el} , the vibrational zero-point energy $U_{vib} = \frac{\hbar\omega}{2}$, and the pressure-volume contribution $pV = k_B T$, to obtain the complete expression for the Gibbs free energy, which we plot in Fig. 6 together with that of the elementary allotropes of the solids in this study.

Appendix C: Systematic Errors

This section examines sources of systematic errors in this study. Fig. 7 compares calculated and experimental entropies for elementary solid phases, where the good agreement indicates that neglecting electronic entropy has a minor impact. Notable but small discrepancies arise when materials transition from solids to liquids. Fig. 8 makes a similar comparison for the gaseous F₂ phase, with generally excellent agreement. In Fig. 9, we investigate the entropy of selected ionic compounds, and also include a comparison of the Gibbs free energy of formation $\Delta_f G$. While the entropy is in line with experiments, we observe well-known systematic deviations in $\Delta_f G$ [56], amounting to an overestimation of approximately 10 % compared to reference values [57]. The error is even more substantial for solids like Li₃AlF₆, which exhibit complex behavior due to multiple phase transitions.

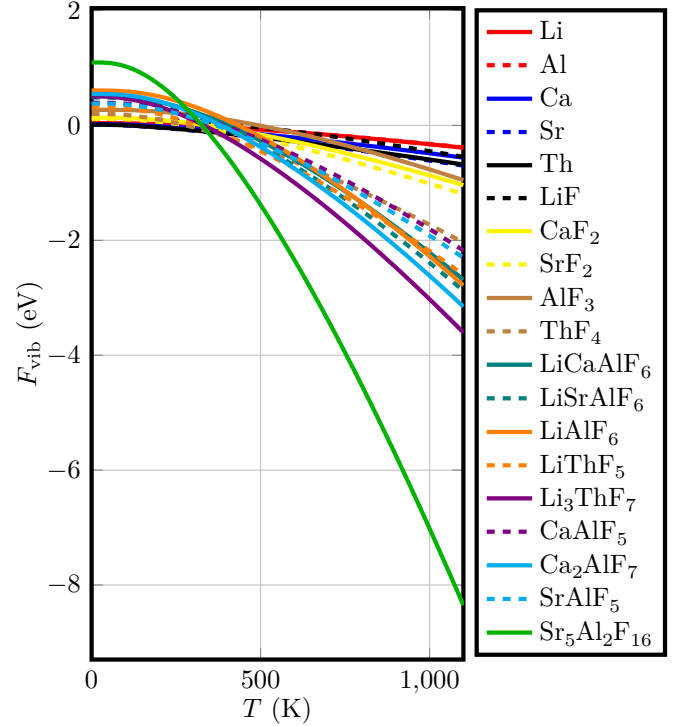


FIG. 4. Vibrational Helmholtz free energy per formula unit for the compounds considered in this study.

When calculating vibrational properties, we use the mass of thorium-232 instead of the relevant thorium isotope. We evaluate the impact of this approximation by comparing the vibrational free energy of ThF₄ for both masses. The difference is negligible, with maximum de-

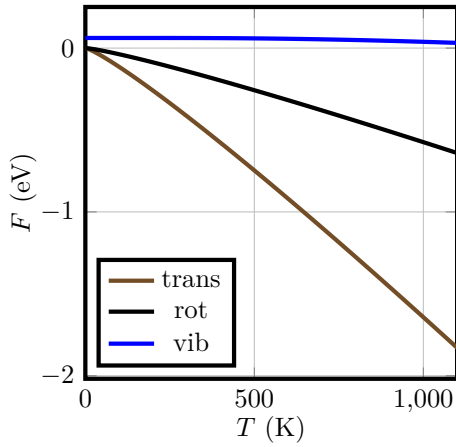


FIG. 5. Translational, rotational and vibrational contributions to the F_2 Helmholtz free energy.

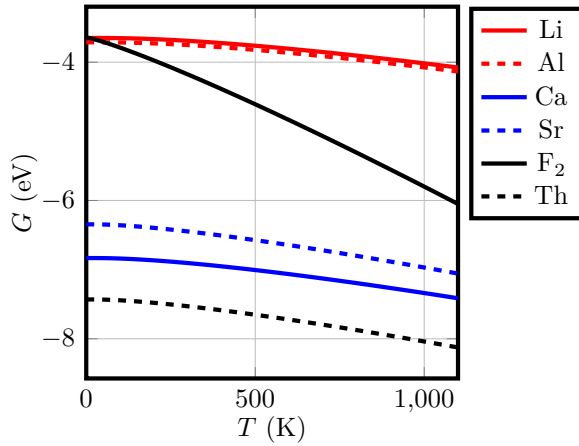


FIG. 6. Gibbs free energy of the elements $G_i[\text{metal}] = \mu_i$ and $\frac{1}{2}G_{F_2}[\text{gas}] = \mu_F$. Note the inclusion of the pseudopotential reference energies.

viations below 2 meV per formula unit at 1100 K.

-
- [1] B. Maheshwari and A. K. Jain, Nuclear isomers at the extremes of their properties, *The European Physical Journal Special Topics* **233**, 1101 (2024).
 - [2] C. Zhang, T. Ooi, J. S. Higgins, *et al.*, Frequency ratio of the ^{229}Th nuclear isomeric transition and the ^{87}Sr atomic clock, *Nature* **633**, 63 (2024).
 - [3] P. G. Thirolf, B. Seiferle, and L. von der Wense, The ^{229}Th isomer: doorway to the road from the atomic clock to the nuclear clock, *Journal of Physics B: Atomic, Molecular and Optical Physics* **52**, 203001 (2019).
 - [4] L. von der Wense and B. Seiferle, The ^{229}Th isomer: prospects for a nuclear optical clock, *The European Physical Journal A* **56**, 10.1140/epja/s10050-020-00263-0 (2020).
 - [5] P. G. Thirolf, S. Kraemer, D. Moritz, and K. Scharl, The thorium isomer ^{229m}Th : review of status and perspectives after more than 50 years of research, *The European Physical Journal Special Topics* **233**, 1113 (2024).
 - [6] E. Peik and C. Tamm, Nuclear laser spectroscopy of the 3.5 eV transition in ^{229}Th , *Europhysics Letters (EPL)* **61**, 181 (2003).
 - [7] C. J. Campbell, A. G. Radnaev, A. Kuzmich, *et al.*, Single-ion nuclear clock for metrology at the 19th decimal place, *Physical Review Letters* **108**, 10.1103/physrevlett.108.120802 (2012).
 - [8] K. Beeks, T. Sikorsky, T. Schumm, *et al.*, The thorium-229 low-energy isomer and the nuclear clock, *Nature Reviews Physics* **3**, 238 (2021).
 - [9] J. C. Berengut and V. V. Flambaum, Testing time-variation of fundamental constants using a ^{229}Th nuclear clock, *Nuclear Physics News* **20**, 19 (2010).
 - [10] M. S. Safronova, The search for variation of fundamental constants with clocks, *Annalen der Physik* **531**, 10.1002/andp.201800364 (2019).
 - [11] P. Fadeev, J. C. Berengut, and V. V. Flambaum, Sensitivity of ^{229}Th nuclear clock transition to variation of the fine-structure constant, *Physical Review A* **102**, 10.1103/physreva.102.052833 (2020).

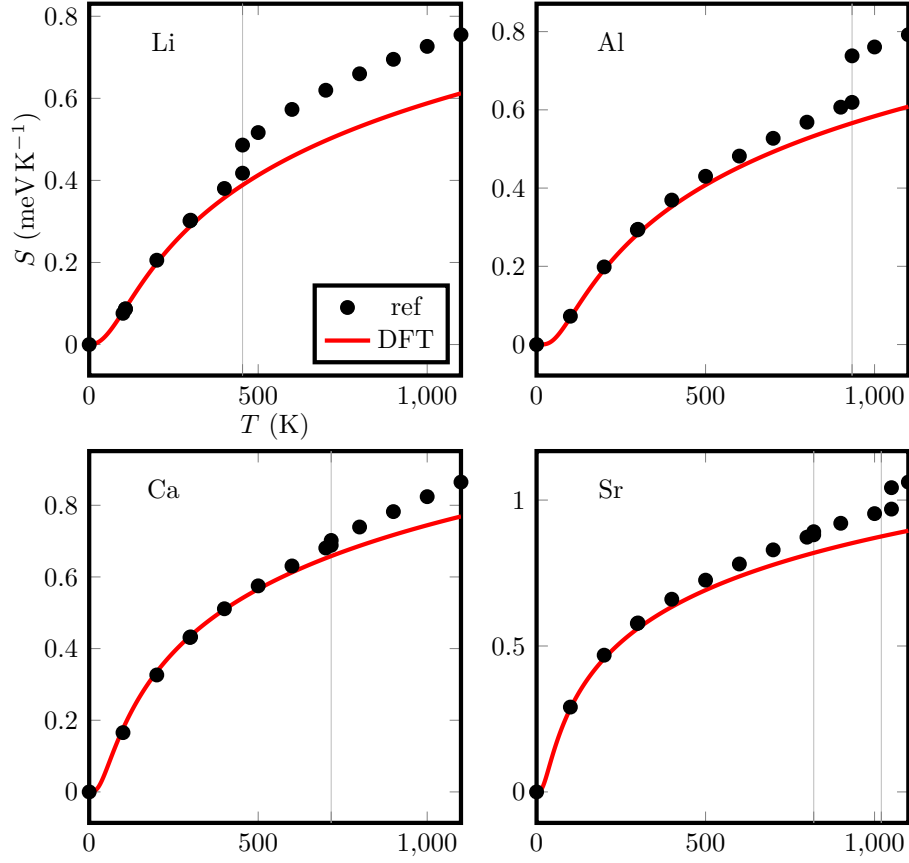


FIG. 7. Comparison of calculated entropy to experimental reference values [57]. Highlighted features include phase transitions between crystalline and liquid phases for Li and Al, as well as transitions between α and β phases for Ca and Sr. Additionally, the temperature range of interest shows a crystal-liquid transition in Sr metal occurring close to its upper limit.

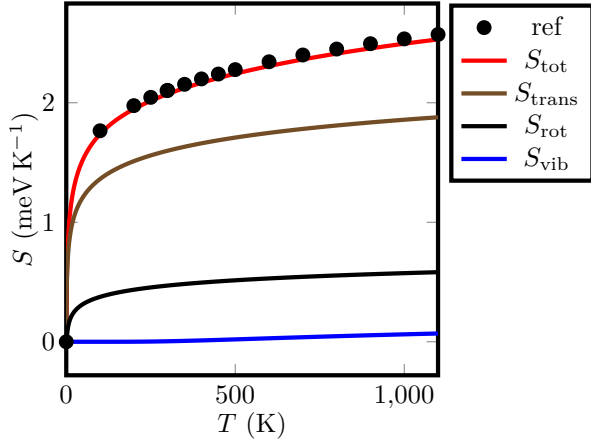


FIG. 8. Comparison of the calculated translational, rotational, and vibrational contributions to the entropy of F_2 and the experimental reference [57].

- [12] E. Peik, T. Schumm, M. S. Safronova, *et al.*, Nuclear clocks for testing fundamental physics, *Quantum Science and Technology* **6**, 034002 (2021).
- [13] A. Caputo, D. Gazit, H.-W. Hammer, *et al.*, On the

- sensitivity of nuclear clocks to new physics, (2024), arXiv:2407.17526v1 [hep-ph].
- [14] V. Goncharov and M. C. Heaven, Spectroscopy of the ground and low-lying excited states of tho^+ , *The Journal of Chemical Physics* **124**, 10.1063/1.2167356 (2006).
- [15] G. A. Kazakov, A. N. Litvinov, V. I. Romanenko, *et al.*, Performance of a $^{229}thorium$ solid-state nuclear clock, *New Journal of Physics* **14**, 083019 (2012).
- [16] M. P. Hehlen, R. R. Greco, W. G. Rellergert, *et al.*, Optical spectroscopy of an atomic nucleus: Progress toward direct observation of the 229th isomer transition, *Journal of Luminescence* **133**, 91 (2013).
- [17] J. Tiedau, M. Okhapkin, K. Zhang, *et al.*, Laser excitation of the $th-229$ nucleus, *Physical Review Letters* **132**, 10.1103/physrevlett.132.182501 (2024).
- [18] R. Elwell, C. Schneider, J. Jeet, *et al.*, Laser excitation of the $th-229$ nuclear isomeric transition in a solid-state host, *Physical Review Letters* **133**, 10.1103/physrevlett.133.013201 (2024).
- [19] S. V. Pineda, P. Chhetri, S. Bara, *et al.*, Radiative decay of the $th-229$ nuclear clock isomer in different host materials, *Physical Review Research* **7**, 10.1103/physrevresearch.7.013052 (2025).
- [20] P. Dessovic, P. Mohn, R. A. Jackson, G. Winkler, M. Schreitl, G. Kazakov, and T. Schumm, $^{229}thorium$ -doped calcium fluoride for nuclear laser spectroscopy,

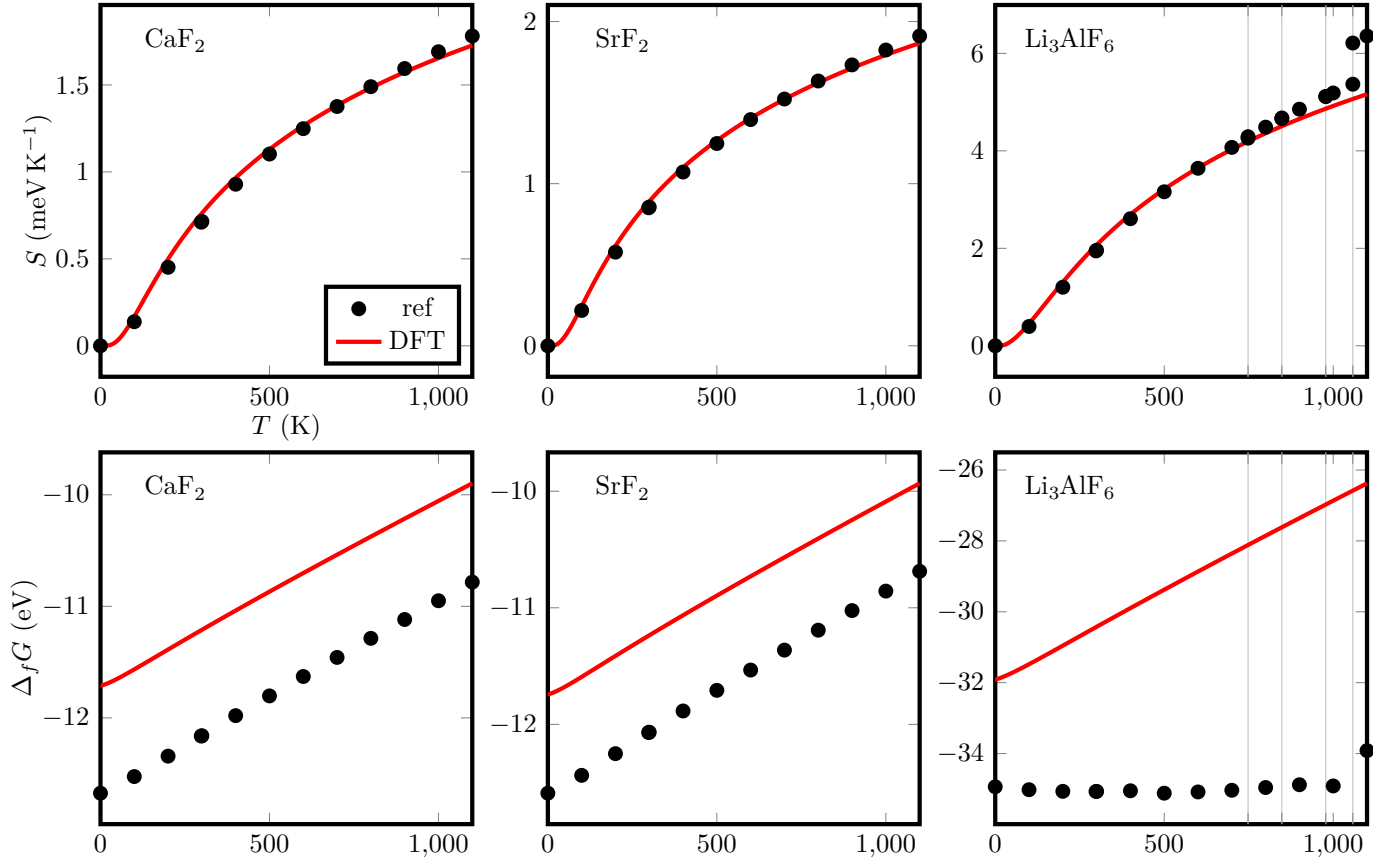


FIG. 9. Entropy comparison of the compounds CaF_2 , SrF_2 and Li_3AlF_6 between calculated values in this study, S^{vib} , and experimental reference data [57]. Li_3AlF_6 undergoes several phase transitions: $\beta \rightarrow \gamma$ at 748 K, $\gamma \rightarrow \delta$ at 848 K, $\delta \rightarrow \varepsilon$ at 978 K, and $\varepsilon \rightarrow \text{liquid}$ at 1058 K.

- Journal of Physics: Condensed Matter **26**, 105402 (2014).
- [21] M. Pimon, J. Gugler, P. Mohn, G. A. Kazakov, N. Mauser, and T. Schumm, Dft calculation of $\text{Th}_{0.229}\text{Mg}_{0.771}\text{F}_3$ for nuclear laser spectroscopy, Journal of Physics: Condensed Matter **32**, 255503 (2020).
- [22] M. Pimon, A. Grüneis, P. Mohn, and T. Schumm, Ab-initio study of calcium fluoride doped with heavy isotopes, Crystals **12**, 10.3390/cryst12081128 (2022).
- [23] R. A. Jackson, J. B. Amaral, M. E. G. Valerio, *et al.*, Computer modelling of thorium doping in LiCaAlF_6 and LiSrAlF_6 : application to the development of solid state optical frequency devices, Journal of Physics: Condensed Matter **21**, 325403 (2009).
- [24] M. Pimon, P. Mohn, and T. Schumm, Band gap calculations for thorium-doped LiCaF , Advanced Theory and Simulations **5**, 10.1002/adts.202200185 (2022).
- [25] C. Freysoldt, B. Grabowski, T. Hickel, J. Neugebauer, G. Kresse, A. Janotti, and C. G. Van de Walle, First-principles calculations for point defects in solids, Reviews of Modern Physics **86**, 253 (2014).
- [26] S. P. Ong, S. Cholia, A. Jain, M. Brafman, D. Gunter, G. Ceder, and K. A. Persson, The materials application programming interface (api): A simple, flexible and efficient api for materials data based on representational state transfer (rest) principles, Computational Materials Science **97**, 209 (2015).
- [27] A. Jain, S. P. Ong, G. Hautier, W. Chen, W. D. Richards, S. Dacek, S. Cholia, D. Gunter, D. Skinner, G. Ceder, and K. A. Persson, Commentary: The materials project: A materials genome approach to accelerating materials innovation, APL Materials **1**, 10.1063/1.4812323 (2013).
- [28] S. P. Ong, W. D. Richards, A. Jain, G. Hautier, M. Kocher, S. Cholia, D. Gunter, V. L. Chevrier, K. A. Persson, and G. Ceder, Python materials genomics (pymatgen): A robust, open-source python library for materials analysis, Computational Materials Science **68**, 314 (2013).
- [29] D. Zagorac, H. Müller, S. Ruehl, J. Zagorac, and S. Rehme, Recent developments in the inorganic crystal structure database: theoretical crystal structure data and related features, Journal of Applied Crystallography **52**, 918 (2019).
- [30] C. J. Bartel, A. Trewartha, Q. Wang, A. Dunn, A. Jain, and G. Ceder, A critical examination of compound stability predictions from machine-learned formation energies, npj Computational Materials **6**, 10.1038/s41524-020-00362-y (2020).
- [31] D. Klimm, G. Lacayo, and P. Reiche, Growth of $\text{cr} : \text{LiCaAlF}_6$ and $\text{cr} : \text{LiSrAlF}_6$ by the czochralski method, Journal of Crystal Growth **210**, 683 (2000).
- [32] K. Beeks, T. Sikorsky, V. Rosecker, M. Pressler,

- F. Schaden, D. Werban, N. Hosseini, L. Rudischer, F. Schneider, P. Berwian, J. Friedrich, D. Hainz, J. Welch, J. H. Sterba, G. Kazakov, and T. Schumm, Growth and characterization of thorium-doped calcium fluoride single crystals, *Scientific Reports* **13**, 10.1038/s41598-023-31045-5 (2023).
- [33] A. Togo, L. Chaput, T. Tadano, and I. Tanaka, Implementation strategies in phonopy and phono3py, *Journal of Physics: Condensed Matter* **35**, 353001 (2023).
- [34] A. Togo, First-principles phonon calculations with phonopy and phono3py, *Journal of the Physical Society of Japan* **92**, 012001 (2023), <https://doi.org/10.7566/JPSJ.92.012001>.
- [35] T. Prohaska, J. Irrgeher, J. Benefield, J. K. Böhlke, L. A. Chesson, T. B. Coplen, T. Ding, P. J. H. Dunn, M. Gröning, N. E. Holden, H. A. J. Meijer, H. Moossen, A. Possolo, Y. Takahashi, J. Vogl, T. Walczyk, J. Wang, M. E. Wieser, S. Yoneda, X.-K. Zhu, and J. Meija, Standard atomic weights of the elements 2021 (iupac technical report), *Pure and Applied Chemistry* **94**, 573 (2022).
- [36] K. Beeks, T. Sikorsky, F. Schaden, M. Pressler, F. Schneider, B. N. Koch, T. Pronebner, D. Werban, N. Hosseini, G. Kazakov, J. Welch, J. H. Sterba, F. Kraus, and T. Schumm, Optical transmission enhancement of ionic crystals via superionic fluoride transfer: Growing vuv-transparent radioactive crystals, *Physical Review B* **109**, 10.1103/physrevb.109.094111 (2024).
- [37] R. M. Pick, M. H. Cohen, and R. M. Martin, Microscopic theory of force constants in the adiabatic approximation, *Physical Review B* **1**, 910 (1970).
- [38] X. Gonze, J.-C. Charlier, D. Allan, and M. Teter, Interatomic force constants from first principles: The case of α -quartz, *Physical Review B* **50**, 13035 (1994).
- [39] X. Gonze and C. Lee, Dynamical matrices, born effective charges, dielectric permittivity tensors, and interatomic force constants from density-functional perturbation theory, *Physical Review B* **55**, 10355 (1997).
- [40] G. Kresse and J. Hafner, Ab initio molecular dynamics for liquid metals, *Phys. Rev. B* **47**, 558 (1993).
- [41] G. Kresse and J. Hafner, Ab initio molecular-dynamics simulation of the liquid-metal–amorphous-semiconductor transition in germanium, *Phys. Rev. B* **49**, 14251 (1994).
- [42] G. Kresse and J. Furthmüller, Efficiency of ab-initio total energy calculations for metals and semiconductors using a plane-wave basis set, *Computational Materials Science* **6**, 15 (1996).
- [43] G. Kresse and J. Furthmüller, Efficient iterative schemes for ab initio total-energy calculations using a plane-wave basis set, *Phys. Rev. B* **54**, 11169 (1996).
- [44] G. Kresse and D. Joubert, From ultrasoft pseudopotentials to the projector augmented-wave method, *Phys. Rev. B* **59**, 1758 (1999).
- [45] J. P. Perdew, K. Burke, and M. Ernzerhof, Generalized gradient approximation made simple, *Physical Review Letters* **77**, 3865 (1996).
- [46] S. P. Huber, S. Zoupanos, M. Uhrin, L. Talirz, L. Kahle, R. Häuselmann, D. Gresch, T. Müller, A. V. Yakutovich, C. W. Andersen, F. F. Ramirez, C. S. Adorf, F. Gargiulo, S. Kumbhar, E. Passaro, C. Johnston, A. Merkys, A. Cepellotti, N. Mounet, N. Marzari, B. Kozinsky, and G. Pizzi, Aiida 1.0, a scalable computational infrastructure for automated reproducible workflows and data provenance, *Scientific Data* **7**, 10.1038/s41597-020-00638-4 (2020).
- [47] M. Uhrin, S. P. Huber, J. Yu, N. Marzari, and G. Pizzi, Workflows in aiida: Engineering a high-throughput, event-based engine for robust and modular computational workflows, *Computational Materials Science* **187**, 110086 (2021).
- [48] G. Pizzi, A. Cepellotti, R. Sabatini, N. Marzari, and B. Kozinsky, Aiida: automated interactive infrastructure and database for computational science, *Computational Materials Science* **111**, 218 (2016).
- [49] aiida-vasp, <https://github.com/aiida-vasp/aiida-vasp>.
- [50] L. Bastonero and N. Marzari, Automated all-functionals infrared and raman spectra (2023).
- [51] A. Togo and I. Tanaka, First principles phonon calculations in materials science, *Scripta Materialia* **108**, 1 (2015).
- [52] F. Kröger and H. Vink, Relations between the concentrations of imperfections in crystalline solids (Elsevier, 1956) pp. 307–435.
- [53] B. S. Nickerson, M. Pimon, P. V. Bilous, J. Gugler, K. Beeks, T. Sikorsky, P. Mohn, T. Schumm, and A. Pálffy, Nuclear excitation of the ^{229}Th isomer via defect states in doped crystals, *Phys. Rev. Lett.* **125**, 032501 (2020).
- [54] B. S. Nickerson, M. Pimon, P. V. Bilous, J. Gugler, G. A. Kazakov, T. Sikorsky, K. Beeks, A. Grüneis, T. Schumm, and A. Pálffy, Driven electronic bridge processes via defect states in ^{229}Th -doped crystals, *Phys. Rev. A* **103**, 053120 (2021).
- [55] T. Kirschbaum, M. Pimon, A. Grüneis, T. Schumm, and A. Pálffy, Electronic Bridge processes in ^{229}Th -doped LiCAF and LiSAF, *arXiv preprint arXiv:2507.05070* (2025).
- [56] S. Kirklin, J. E. Saal, B. Meredig, A. Thompson, J. W. Doak, M. Aykol, S. Rühl, and C. Wolverton, The open quantum materials database (oqmd): assessing the accuracy of dft formation energies, *npj Computational Materials* **1**, 10.1038/npjcompumats.2015.10 (2015).
- [57] Thomas C. Allison, Nist-janaf thermochemical tables - srd 13 (2013).